Cephalopod coloration model. I. Squid chromatophores and iridophores

Richard L. Sutherland,[1,2,*] Lydia M. Mäthger,[3] Roger T. Hanlon,[3] Augustine M. Urbas,[1] and Morley O. Stone[1]

[1]*Air Force Research Laboratory, 3005 Hobson Way, Wright-Patterson Air Force Base, Ohio 45433-7707, USA*
[2]*Science Applications International Corporation, 4031 Colonel Glenn Highway, Dayton, Ohio 45431, USA*
[3]*Marine Resources Center, Marine Biological Laboratory, 7 MBL Street, Woods Hole, Massachusetts 02543, USA*
**Corresponding author: sutherlandr@saic.com*

Received September 11, 2007; revised November 28, 2007; accepted December 3, 2007;
posted December 21, 2007 (Doc. ID 87405); published February 7, 2008

We have developed a mathematical model of skin coloration in cephalopods, a class of aquatic animals. Cephalopods utilize neurological and physiological control of various skin components to achieve active camouflage and communication. Specific physical processes of this coloration are identified and modeled, utilizing available biological materials data, to simulate active spectral changes in pigment-bearing organs and structural iridescent cells. Excellent agreement with *in vitro* measurements of squid skin is obtained. A detailed understanding of the physical principles underlying cephalopod coloration is expected to yield insights into the behavioral ecology of these animals. © 2008 Optical Society of America

OCIS codes: 000.1430, 050.7330, 160.1435, 240.0310, 260.3160, 330.1690.

1. INTRODUCTION

Color is an important and ubiquitous property in biology. Although animal pigments have long been studied, structural coloration in biology has become a subject of recent intense interest, with many examples of exotic photonic structures discovered in both aquatic and terrestrial systems [1–3]. Since most animals are visual, color plays a significant role in, for example, predator–prey relationships, mating, and the generation of visual signals between conspecific or interspecific animals. A crucial defense mechanism for many animals is camouflage. Cephalopods—a class of aquatic invertebrates (Phylum Mollusca) that includes squid, octopus, and cuttlefish—have developed a highly sophisticated system of dynamic camouflage [4,5]. They adapt their color and body pattern to various visual features of the immediate background. Color is controlled through a combination of *both* pigments and photonic structures in an elaborate skin configuration. This produces a rich repertoire of spectra and patterns that is highly adaptive to changing backgrounds and situations. Current biological research is focused on understanding how cephalopods neurologically perform these adaptations [6–9].

Although cephalopod skin has been widely studied and characterized biologically, there has been relatively little work done in modeling its optical properties. Masthay presented a quantitative model of pigment absorption in animals, including cephalopods, based solely on Beer's law, but did not include scattering or diffuse reflection [10]. Denton and Land discussed the mechanism of iridescent reflections from fish and cephalopods in terms of quarter-wave thin-film stacks [11], and Mäthger and Denton described theoretical calculations of spectra that they related qualitatively to the iridescence of loliginid squid [12]. In none of these previous works, however, were detailed calculations of spectra compared quantitatively to experimental spectra or combined to illustrate coloration effects in different environments.

Our objective is to provide answers to questions such as the following: Given a particular light source, what does a patch of cephalopod skin look like to an observer? Particularly, what is the color rendition of the skin in a spatial resolution element (i.e., a pixel)? What are the physical properties of the skin that lead to this coloration? In answering such questions we must consider the multiple optical interactions of various skin components (pigments and structural elements), which can undergo physiological or neurological modification, and the fact that within an aquatic environment the nature of ambient light can range from highly collimated to diffuse. Results of this study should enhance our understanding of how these animals employ dynamic camouflage to adapt to their background.

We have developed a model of the reflective properties for a generic cephalopod skin consisting of any number of layers with various optical elements, both structural and pigmented. The model incorporates multiple internal reflections among the various skin components and consists also of various submodels describing the optical properties of each skin element individually. In this paper we present these submodels for two components, namely, the pigmented chromatophores and the structural iridophores, for which the spectral reflectance and transmittance can be changed by the animal, either neurologically or physiologically, to achieve dynamic camouflage. We compare these models with *in vitro* experimental measurements of skin components in squid. Materials properties, such as index of refraction, absorption and scattering coefficients, and dispersion are obtained either from the literature or through comparison of the models with experimental data. A future paper will combine these results with those of submodels for static skin components

to investigate multilayer effects on the total animal reflectance with a generic cephalopod skin.

2. THEORY

The topmost layers of a squid skin are pigment-bearing organs called chromatophores. Each chromatophore comprises a sacculus containing pigment granules of a specific color (brown, red, or yellow) and surrounded by a series of radial muscles. When the muscles contract, the sacculus is expanded, thus spreading out the pigment granules. The sacculus is elastic so that when the muscles relax, the chromatophore retracts. The pigment colors are ordered, going from yellow to red to brown in skin depth [9]. Subjacent to the chromatophores are structural color elements called iridophores. These consist of several iridosomes that have a multilayer structure consisting of thin, transparent protein platelets [13] sandwiched between spacers of cytoplasm. The iridophores produce iridescent colors upon illumination by white light. The intensity and color of iridophores can change in the presence of the neuromodulator acetylcholine [14].

Ultimately, we wish to relate the various components of radiant flux (both collimated and diffuse) at the boundaries of the various skin layers. To this end we define the partial reflectances and transmittances for each layer. By partial we mean the reflectance or transmittance that would be measured in an experiment for a completely isolated layer using either pure collimated or pure diffuse light, and separately detecting specularly and diffusely reflected or transmitted light. For example, if we designate $J_{d\leftarrow c}$ as the diffuse component of the total reflected light for a purely collimated input I_c, then the ratio $R_{cd}=J_{d\leftarrow c}/I_c$ is the partial reflectance. A similar definition holds for the partial transmittance T_{cd}. We also define partial reflectance and transmittance for collimated light produced from collimated light (R_{cc} and T_{cc}) and diffuse light produced from diffuse light (R_{dd} and T_{dd}).

For the models presented here we have made some simplifying assumptions. All elements, as well as the entire skin itself, are embedded in a watery environment. Hence we can ignore interfacial Fresnel reflections except those that arise from components of interest. These include specular reflections from iridophores and scattering from pigment granules. The scattering elements are taken to behave as ideal Lambertian surfaces, yielding only diffuse reflectance. They do, however, have some specular transmittance (i.e., regular transmittance, light that is neither absorbed nor scattered) as well as diffuse transmittance. Therefore, specular reflection arises only from smooth photonic structural elements. We assume that there are no index heterogeneities in these components. Therefore, they have diffuse reflectance or transmittance only when irradiated by diffuse light.

A. Chromatophore Layers

The pigment granules of chromatophores absorb and scatter light. We thus define absorption and scattering coefficients α and σ, respectively, both having units of inverse length. (We note that these parameters are commonly designated by a and b, respectively, in the ocean optics community [15].) To distinguish forward and backward scattering, we introduce the forward scattering ratio ξ, which is defined as the ratio of light scattered into the forward hemisphere to the total scattered light [16].

We treat the chromatophore ideally as a disk of uniform thickness d and elliptical cross section. Electron microscopy data for an expanded chromatophore indicate that a typical pigment granule size is $\sim$300 nm and the mean center-to-center spacing of granules is $>$300 nm [17]. Applying the standard Rayleigh criterion, the chromatophore would be optically smooth if $\delta h<\lambda/8n$, where δh is the root-mean-square roughness height measured from some reference plane, which would imply $\delta h<55$ nm for $\lambda=600$ nm and $n=1.33$. Since the surface is not optically smooth, we make the simplifying assumption that $R_{cc}\approx 0$. Although this does not entirely rule out the presence of a specular component, it is likely to be small and not contribute significantly to the total skin reflectance. Hence we consider a model for the isolated chromatophore as illustrated in Fig. 1. Let a prime symbol indicate the derivative with respect to z, where z is the distance measured from the front of the chromatophore (see Fig. 1). Designating I as the forward flux and J as the backward flux, the radiation transport equations may then be written as [16]

$$I_c' = -(\alpha+\sigma)I_c, \tag{1a}$$

$$I_d' = -\eta\alpha I_d - \eta(1-\xi)\sigma I_d + \eta(1-\xi)\sigma J_d + \xi\sigma I_c, \tag{1b}$$

$$J_d' = \eta\alpha J_d + \eta(1-\xi)\sigma J_d - \eta(1-\xi)\sigma I_d - (1-\xi)\sigma I_c, \tag{1c}$$

which is a variant of the Kubelka–Munk model [18]. In Eqs. (1b) and (1c) we have introduced the effective path length coefficient η for diffuse light, defined by $\eta=\langle 1/\cos\theta\rangle$, where θ is an angle of propagation with respect to the z axis and the brackets indicate an average over the full solid angle in the forward direction weighted by the angular distribution of the diffuse radiation [16,18]. Note that I_c represents the flux of ballistic (unscattered) photons and thus has an effective path length coefficient of one.

This system of coupled differential equations constitutes what is known as a three-flux model and may be solved exactly. The solutions are similar in many respects to those for the two-flux model (forward and backward diffuse light flux only) given by Kubelka [18], and the four-flux model (forward and backward collimated and diffuse light flux) given by Maheu *et al.* [16]. In both of these earlier works reflection from a background was also included. This type of reflection is ignored here since we are considering an isolated chromatophore. Appendix A gives the detailed solution of this particular three-flux model,

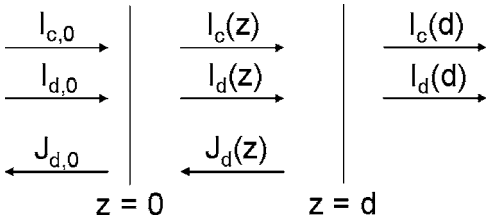

Fig. 1. Three-flux model for computing transmittance and reflectance of a chromatophore.

which differs to some extent from these previous developments. The results for the collimated–collimated and diffuse–diffuse components are simple:

$$T_{cc} = \exp[-(\alpha + \sigma)d], \tag{2}$$

$$T_{dd} = \frac{\kappa}{\kappa \cosh \eta\kappa d + [\alpha + (1-\xi)\sigma]\sinh \eta\kappa d}, \tag{3}$$

$$R_{dd} = \frac{(1-\xi)\sigma \sinh \eta\kappa d}{\kappa \cosh \eta\kappa d + [\alpha + (1-\xi)\sigma]\sinh \eta\kappa d}, \tag{4}$$

where

$$\kappa = \sqrt{\alpha^2 + 2(1-\xi)\sigma\alpha}. \tag{5}$$

The results for the collimated–diffuse components can be expressed analytically but are rather complex. They may be simplified, however, by using an approximation. For pure collimated light incident on a particle with size comparable to or greater than the wavelength of light, the scattering is peaked sharply in the forward direction, and the effective path length coefficient is not much larger than one [16]. Typical pigment granule size is ~300 nm [17]. Hence for visible collimated light we make the approximation $\eta \approx 1$. Then the expressions for the collimated–diffuse components reduce to (see Appendix A)

$$T_{cd} \approx \frac{\kappa}{\kappa \cosh \kappa d + [\alpha + (1-\xi)\sigma]\sinh \kappa d} - \exp[-(\alpha + \sigma)d], \tag{6}$$

$$R_{cd} \approx \frac{(1-\xi)\sigma \sinh \kappa d}{\kappa \cosh \kappa d + [\alpha + (1-\xi)\sigma]\sinh \kappa d}. \tag{7}$$

Note that we do not make the same approximation in Eqs. (3) and (4) since, by definition, incident diffuse light is already propagating in multiple directions. For isotropic diffuse light, $\eta = 2$ (see, for example, [18]).

In laboratory experiments the incident light is purely collimated, and R_{cd} and $T = T_{cc} + T_{cd}$ are measured for near-normal incidence. Forming the quantities a and b in terms of measured parameters

$$a = \frac{1 + R_{cd}^2 - T^2}{2R_{cd}},$$

$$b = \sqrt{a^2 - 1}. \tag{8}$$

Equations (2) and (5)–(7) may be used to extract the backward scattering and absorption coefficients of the pigment. These are often referred to in the literature as S and K [19]. The results are

$$S \equiv (1-\xi)\sigma = \frac{1}{bd}\sinh^{-1}\left(\frac{bR_{cd}}{T}\right), \tag{9}$$

and

$$K \equiv \alpha = (1-a)S. \tag{10}$$

Since the chromatophores are characterized *in vitro*, the thickness is not known. Consequently, the experimentally determined parameters are in the form of products Sd and Kd, where S and K are proportional to pigment concentration and hence inversely proportional to the volume of the sacculus. Although the volume, and hence the pigment concentration, is conserved as the sacculus expands (i.e., S and K are constants), the path length d is reduced, producing changes in the reflectance and transmittance as indicated by the explicit dependence of Eqs. (2)–(4), (6), and (7) on d. Consequently, the extracted experimental parameters Sd and Kd are inversely proportional to the cross sectional area of the chromatophores. For constant volume, the cross sectional area and thickness are reciprocally related, and an increase in one by some factor results in a decrease in the other by the same factor. Assuming that the shape of the chromatophore remains an elliptical disk as its volume changes, we introduce a scaling factor ρ for the radius (or geometric mean radius) of the elliptical cross section. Therefore, to simulate expansion and retraction of the chromatophore, which dynamically changes the reflectance and transmittance, the parameters Sd and Kd are scaled as ρ^{-2}. The default parameters ($\rho = 1$) are determined by the size of the chromatophores for which R_{cd} and T are measured.

Finally, note that the total scattering coefficient is needed for calculating T_{cc} and is given by $\sigma = S/(1-\xi)$. Hence, values for the forward scattering ratio must be assumed for modeling purposes. Some guidance for selecting these values may be found in the literature [16,20]. Vargus and Kinlasson give numerical methods for estimating the forward scattering ratio based on particle size and complex index of refraction using Lorenz–Mie theory [21].

B. Iridophore Layer

Iridophores consist of stacked layers of iridosomes, which themselves comprise 2–10 layers of thin protein platelets separated by thin layers of cytoplasm. The platelets are composed of a recently identified protein family named reflectins [13], which are found in the iridophores of certain squid. Platelets have been studied by electron microscopy, and a typical thickness is ~100 nm. Cytoplasmic spacer thickness is of the same order [22]. Reflectin has been recombinantly expressed and cast as thin films. A refractive index of 1.591 has been measured using a prism coupling technique [23]. The refractive index of cytoplasm is 1.33, similar to that of water [11]. Iridosomes are tightly packed in the iridophore cell and thus approximate a thin film, high–low-index multilayer stack with Bragg reflection in the visible or near-infrared spectral regions. Large numbers of Bragg reflectors are situated in the iridophore layer, forming iridescent splotches in the skin [6,14].

Iridophores have been shown to have properties similar to that of quarter-wave stacks [11,12], although the detailed spectra have not been previously modeled. Close examination of iridophore micrographs reveals that, although the platelets have reasonably uniform thickness, the cytoplasm spacers do not [23]. Moreover, the platelets are not ideally flat but exhibit some small, apparently random curvature. Hence, to model these reflectors we first calculate reflectance and transmittance by approximating them as ideal multilayer thin-film stacks using standard methods and then modify the results to include

the effects of their random structure. We thus treat an entire iridophore (consisting of one or more iridosomes) as a single multilayer stack, employing a 2×2 matrix approach to calculate the forward and backward propagating electric field amplitudes [24], the results of which we summarize next.

The incident and reflected field amplitudes, E_0 and E_r, respectively, expressed in a column vector, may be related to the transmitted field amplitude, E_t, by a 2×2 transfer matrix $\mathbf{P}$:

$$\begin{pmatrix} E_0 \\ E_r \end{pmatrix} = \mathbf{P}\begin{pmatrix} E_t \\ 0 \end{pmatrix}. \tag{11}$$

The multilayer-film (*mf*) reflectance and transmittance are then given by

$$R_{mf} = \left|\frac{E_r}{E_0}\right|^2 = \left|\frac{P_{21}}{P_{11}}\right|^2, \tag{12}$$

$$T_{mf} = \frac{n_s \cos\theta_s}{n_0 \cos\theta_0}\left|\frac{E_t}{E_0}\right|^2 = \frac{n_s \cos\theta_s}{n_0 \cos\theta_0}\left|\frac{1}{P_{11}}\right|^2, \tag{13}$$

where the subscripts 0 and s refer to the input and substrate (exit) media, respectively. We will assume these media to be identical. Also, since $R_{mf}=1-T_{mf}$ (the iridophores are nonabsorbing), we need only focus on the P_{11} element of the transfer matrix.

The multilayer consists of N alternating high-index (H) and low-index (L) pairs having refractive index n_H and n_L and thickness h_H and h_L, respectively. Assuming that each pair in the stack is identical, the transfer matrix can be written in terms of the power of a single matrix $\mathbf{M}$, i.e., $\mathbf{P}=\mathbf{F}_{LH}\mathbf{M}^N\mathbf{F}_{LH}^{-1}$, where $\mathbf{M}$ is the product of four matrices,

$$\mathbf{M} = \mathbf{\Phi}_H\mathbf{F}_{HL}\mathbf{\Phi}_L\mathbf{F}_{LH}. \tag{14}$$

We have taken the input and exit media to have the same refractive index as the low-index film, i.e., similar to water. In the product $\mathbf{M}$ there are two phase matrices, given by

$$\mathbf{\Phi}_k = \begin{bmatrix} \exp(-i2\pi n_k h_k \cos\theta_k/\lambda) & 0 \\ 0 & \exp(+i2\pi n_k h_k \cos\theta_k/\lambda) \end{bmatrix}, \tag{15}$$

where the subscript $k=H$ or L, λ is the wavelength, and θ_k is the angle of propagation with respect to the film-normal in the kth layer; and there are two Fresnel matrices, given by

$$\mathbf{F}_{jk} = \frac{1}{t_{jk}}\begin{bmatrix} 1 & r_{jk} \\ r_{jk} & 1 \end{bmatrix}, \tag{16}$$

where $jk=HL$ or LH, and t_{jk} and r_{jk} are the usual Fresnel transmission and reflection coefficients for the jkth interface, which depend on the polarization of light [25].

To a good approximation, we take the cytoplasm to have an index of refraction like water ($n_w\approx1.33$). The refractive index dispersion of reflectin has been fit to a Cauchy equation, $n_r(\lambda)=A_r+B_r/\lambda+C_r/\lambda^2$, where λ is expressed in nanometers, with $A_r=1.56713$, $B_r=-13.386$ nm, and $C_r=16.290\times10^3$ nm^2 [23]. However, this result was obtained from measurements done on a cast film, whereas *in vivo* the protein is normally in an aqueous solution bound within a cell membrane. In addition, physiologically active squid iridophores have been found to change reversibly from a noniridescent to an iridescent state. These active cells also demonstrate the same response *in vitro* to the neuromodulator acetylcholine. This has been correlated by transmission electron microscopy studies to the physical structure of the platelets. In the iridescent iridophores the platelets are thin and uniformly electron-dense. Noniridescent iridophore platelets exhibit a flocculent or ribbonlike structure containing electron-lucent and electron-dense regions. In addition, the platelet regions are thicker in the noniridescent state [14,22]. We can simulate these properties of the iridophores by assuming reflectin to be in an aqueous solution having some equilibrium volume fraction f_0 of water when the iridophore is maximally iridescent. As the iridophore changes to a noniridescent form, we assume that the platelet region is invaded with a waterlike fluid, swelling the region and creating a new equilibrium volume fraction $f>f_0$. We thus let the high-index region be characterized by a refractive index given by a simple mixture formula,

$$n_H(\lambda) = fn_w(\lambda) + (1-f)n_r(\lambda), \tag{17}$$

and a thickness that changes linearly with the volume fraction of water,

$$h_H = h_0 + \frac{dh}{df}(f-f_0). \tag{18}$$

In this model, h_0 is the equilibrium platelet thickness for volume fraction f_0, and dh/df is the rate that the thickness changes with respect to an increase in the volume fraction of water. Both f_0 and dh/df are treated as phenomenological parameters that can be adjusted to fit experimental data.

Next we incorporate small irregularities into the iridophore structure. Although the platelets are highly ordered, there appears to be some random structure superimposed upon this order. Figure 2 gives a schematic illustration of the platelet shape and spacing irregularity. If we let h_L designate the mean separation of platelets, then the spacer thickness at any point can be given by $h_L+\zeta$, where ζ is a position-dependent (positive or negative) random variable. Furthermore, it appears from electron micrographs that there is no statistical correlation in spacer thickness from layer to layer [26]. Thus, we assume that each spacer is characterized by a statistically independent random variable ζ_k. We also assume that the curvature of the platelet is small everywhere; i.e., although the spacing between platelets changes continuously with position, the rate of change or slope of the platelet surface is very small. Consequently, we take the deviation of any ray trajectory through each layer from that of an ideal, parallel layer stack to be negligibly small. Then the result of the random spacing in the iridophore is to add a random phase $\delta\varphi_k=2\pi n_L\zeta_k\cos\theta_L/\lambda$ to the diagonal elements of each phase matrix $\mathbf{\Phi}_L$ in the transfer matrix $\mathbf{P}$. Since the phase matrix is diagonal, this change

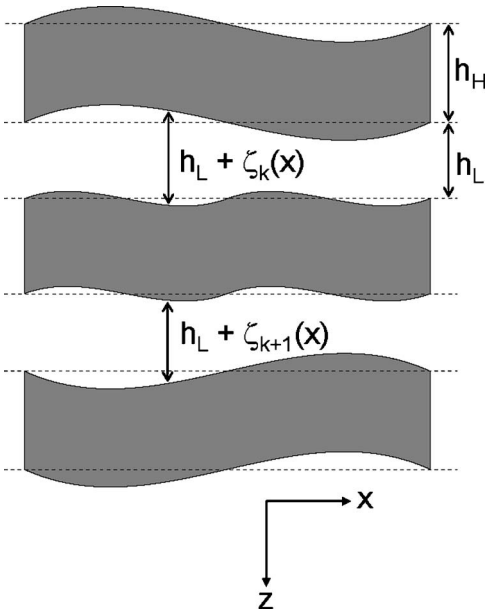

Fig. 2. Schematic illustration of the random spacing of platelets in iridophores. The platelets (dark) have a uniform thickness h_H, while the spacer thickness varies as $h_L+\zeta_k$ for layer k, where $\zeta_k(x)$ is a random variable. A sensor will integrate over the spatial variable x within a pixel and yield a response related to the reflectance (or transmittance) averaged over the random variables. The mean spacer thickness is h_L.

can be accomplished by making the substitution $\mathbf{\Phi}_L \rightarrow \mathbf{D}_k\mathbf{\Phi}_L$ for all N low-index phase matrices in the transfer matrix product $\mathbf{P}$, where

$$\mathbf{D}_k = \begin{bmatrix} \exp(-i\,\delta\varphi_k) & 0 \\ 0 & \exp(+i\,\delta\varphi_k) \end{bmatrix}, \tag{19}$$

and k is now a parameter that runs from 1 to N. Note that under these conditions the transfer matrix can no longer be written in terms of the simple power of a single matrix since each matrix $\mathbf{M}_k$ is different in general and continuously variable across the iridophore.

Everything we have discussed up to this point concerns a single iridophore. However, within a typical spatial resolution element of the observer there will generally be a large ensemble of iridophores making up an iridescent splotch in the iridophore layer. It is unlikely that these iridophores are identical; i.e., they will display some small deviations in Bragg wavelength due to angular or platelet-separation variations. We will account for these differences by assuming a Gaussian distribution of Bragg wavelengths over the iridophore ensemble, which can be accomplished by the introduction of another single random variable ζ_0. Accordingly, we now modify the model by letting any *single* iridophore have a mean spacer thickness given by $h_L+\zeta_0$, where ζ_0 is a random variable over the entire ensemble of iridophores. The mean spacer thickness for the entire ensemble is then h_L.

The transmittance of the iridophore layer now becomes a function of $N+1$ random variables. A sensor will yield a response that is an average of the transmittance (or reflectance) over these variables by integrating spatially across a pixel. Assuming Gaussian statistics for each random variable, we define normalized probability distributions $p(\zeta_0), p(\zeta_1), p(\zeta_2), \ldots, p(\zeta_N)$, all of which have zero means and respective standard deviations $\sigma_0, \sigma_1, \sigma_2, \ldots, \sigma_N$, and we assume that $p(\zeta_k)$ is the same for any iridophore in the ensemble. Then the average collimated–collimated transmittance is given by

$$T_{cc} = \int T_{mf}(\zeta_0, \{\zeta_k\})p(\zeta_0)p(\zeta_1)p(\zeta_2)\ldots \times p(\zeta_N)\mathrm{d}\zeta_0\mathrm{d}\zeta_1\mathrm{d}\zeta_2\ldots\mathrm{d}\zeta_N, \tag{20}$$

where $\{\zeta_k\}$ represents the set of random variables, $k=1\ldots N$, for any single iridophore; T_{cc} is a function of wavelength, angle of incidence, and polarization; and $R_{cc}=1-T_{cc}$. For simplicity, we will assume that $\sigma_k=\sigma_\zeta$ for all $k=1\ldots N$, where σ_ζ is a constant ($\sigma_\zeta \neq \sigma_0$). Therefore, the statistics of the iridophores are characterized by just two parameters. In Appendix B we give an approximate form of Eq. (20) to order σ_ζ^2, which is valid for $\sigma_\zeta \ll \lambda$.

To calculate the diffuse–diffuse components, we assume a Lambertian light source with constant spectral radiance L_λ independent of the angle of propagation. The spectral optical power incident on a point on the surface of the iridophore, having an element of surface area $\mathrm{d}A$, is given by $d^2\Phi_{\lambda,0}=L_\lambda \cos\theta \mathrm{d}A\mathrm{d}\Omega$, where θ is the angle of incidence between the iridophore-normal and a line connecting a point centered on an element $\mathrm{d}A'$ of the light source with the point on the surface of the iridophore, and $d\Omega = \sin\theta\mathrm{d}\theta\mathrm{d}\phi$ is the solid angle subtended by $\mathrm{d}A'$ at the point on the iridophore (ϕ is the azimuth angle). The power transmitted by the iridophore is given by $d^2\Phi_{\lambda,t} = T_{cc}(\lambda,\theta)L_\lambda \cos\theta \sin\theta \mathrm{d}\theta\mathrm{d}\phi\mathrm{d}A$. Dividing by $\mathrm{d}A$ and integrating over the hemispherical solid angle to obtain the spectral (vector) irradiance I_λ (this assumes that the source is large compared to the iridophore), the diffuse–diffuse transmittance is given by the ratio

$$T_{dd}(\lambda) = \frac{I_{\lambda,t}}{I_{\lambda,0}} = \int_0^{\pi/2} T_{cc,u}(\lambda,\theta)\sin 2\theta \mathrm{d}\theta. \tag{21}$$

A similar expression holds for R_{dd}, or one can be computed and the other determined by $R_{dd}+T_{dd}=1$ since there is no absorption. We assume that diffuse light is completely unpolarized. Since T_{cc} and R_{cc} depend on polarization, the collimated–collimated component in the integrand of an expression like Eq. (21) is understood to represent equal contributions of s polarization and p polarization, i.e., $T_{cc,u}=(T_{cc,s}+T_{cc,p})/2$.

Finally, we assume that the iridophore platelets and spacers contain no index heterogeneities. Since the curvature of the platelets is small, so that deviations of ray trajectories are negligible, the iridophores produce very little incoherently scattered light. We thus set $R_{cd}\approx T_{cd}\approx 0$.

3. EXPERIMENT

Skin specimens were prepared from squid (*Loligo pealeii*) for chromatophore and iridophore measurements. Small dissected skin elements were pinned onto the Sylgard-covered dish of a goniometer. The specimens were covered with sea water for preservation of their properties during the measurements. Spectral reflectance and transmittance measurements were obtained using an Ocean Op-

tics fiber optic spectrometer attached to a dissecting microscope. Details of the experimental apparatus and methods can be found in [6].

Spectral transmittance was measured by directing light from the bottom of the sample at normal incidence through the sample and into the microscope. The microscope objective restricted the angle of incidence for reflectance measurements to no less than ~10°. The angle of incidence in water was thus ~7.5°, satisfying near-normal incidence conditions. Reflectance measurements were performed using a black felt background beneath the skin samples. This background produced a very flat spectral reflectance of approximately 0.025 across the visible spectrum. Corrections were made for Fresnel reflections at the air–water and air–Petri-dish interfaces. The measurements recorded were total reflectance and transmittance, i.e., the sum of specular and diffuse components.

4. RESULTS AND DISCUSSION

A. Chromatophores

Reflectance and transmittance spectra were measured for 6–8 chromatophores of each color. Average spectra were then computed for brown, red, and yellow chromatophores, and $K(\lambda)$ and $S(\lambda)$ were extracted from these averages using Eqs. (8)–(10). These spectral properties are plotted in Fig. 3. With these values of $K(\lambda)$ and $S(\lambda)$ we can scale the reflectance and transmittance of individual chromatophores of variable size (area and thickness) using Eqs. (2), (6), and (7) ($\eta \approx 1$) and by adjusting the scale factor ρ. Examples of this scaling for individually selected chromatophores, compared to data, are given in Figs. 4 and 5. We should point out that at present we are limited to this semiempirical method of predicting R and T spectra for the chromatophores based solely on their size, using experimentally extracted K and S values. Detailed modeling from first principles (e.g., Mie theory) would require knowledge of n and k spectra (real and imaginary parts of the complex index of refraction, respectively) for the pigments. This information is not currently unavailable. Although it may appear that the results discussed here are circular, i.e., measured R and T spectra are used to determine K and S spectra, which in turn are used to predict R and T, it is important to note that one cannot simply scale R and T spectra for the varying size of chromatophores. This scaling must be done within the arguments of the hyperbolic functions in Eqs. (3), (4), (6), and (7). Also, it is not possible to compute T_{cc}, Eq. (2), without knowledge of S and K. This becomes particularly important when dealing with multilayer skin effects (e.g., chromatophores over iridophores; see Subsection 4.C), where the specular reflection from underlying elements depends on the specular transmittance of the chromatophores. Moreover, knowledge of S and K spectra also gives us valuable information about the optical properties of the pigments themselves, as we discuss below.

The brown chromatophore exhibits the largest absorption, but we cannot ascertain whether this is due to a larger absorption coefficient, a larger thickness, or both. Its spectrum is similar to that of a melanin pigment. The absorption edges of the red and yellow chromatophores

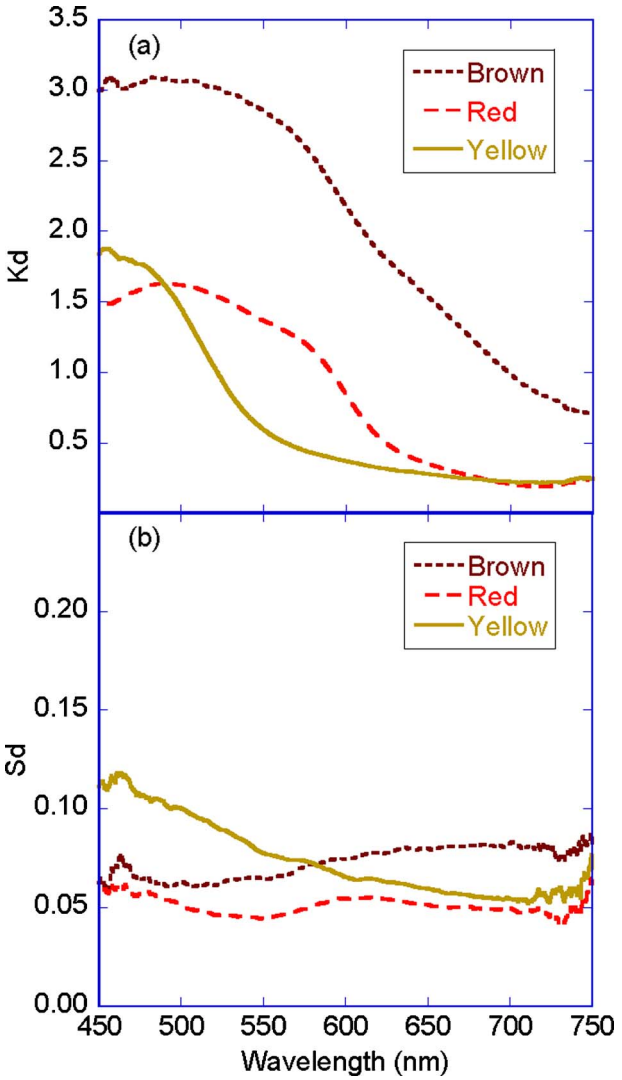

Fig. 3. (Color online) Spectral absorption and backscattering coefficients (normalized to thickness d) derived from reflectance and transmittance measurements of the brown, red, and yellow chromatophores of the squid *Loligo pealeii*. (a) Absorption (K) spectra. (b) Backscattering (S) spectra.

are shifted toward the blue, giving them their characteristic colors. Backscattering coefficient spectra, $S(\lambda)$, for the brown and red chromatophores are fairly flat, rising slightly toward the red end of the spectrum; $S(\lambda)$ for the yellow chromatophore exhibits an inverse dependence on wavelength, more like a typical Mie scatterer. Again, since the absolute thickness of these chromatophores is unknown, we cannot comment on the relative magnitudes of the backscattering coefficients.

It is interesting to compare these S and K spectra to those of inorganic paint pigments. A survey of common colorants is given in [20]. Three of these are visually similar in color to the chromatophores studied here: Red Iron Oxide (brownish), Acra Red, and Cadmium Yellow Light. (Photos of these pigments in [20] can be compared with the color photos of *L. pealeii* chromatophores in [6].) Red Iron Oxide has strong absorption in the blue with a rolloff toward the red beginning at about 550 nm, similar to the $K(\lambda)$ spectrum for the brown chromatophore in Fig. 3(a).

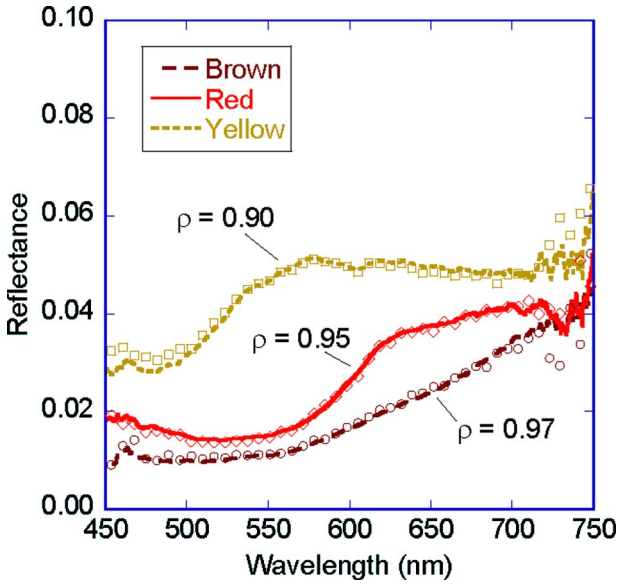

Fig. 4. (Color online) Examples of model fits to specific chromatophore reflectance measurements of the squid *Loligo pealeii* obtained by using K and S values in Fig. 3 and adjusting the scaling parameter ρ.

Likewise, both pigments exhibit a rise in backscattering coefficient at about the same wavelength. However, for Red Iron Oxide $S(\lambda)$ increases by about an order of magnitude between 550 and 600 nm. Clearly, this commercial pigment is designed to yield high reflectance (~30% for a 26 μm thick film [20]), whereas the cephalopod brown chromatophore reflectance is very low, typically <2% [6]. Acra Red and the squid red chromatophore both exhibit a maximum absorption in the visible at ~500 nm. They both also display a relative minimum in $S(\lambda)$ at ~550 nm followed by a relative maximum at ~600 nm. However, $S(\lambda)$ changes by about a factor of 5 in this spectral range for Acra Red compared to the approximate 10% change

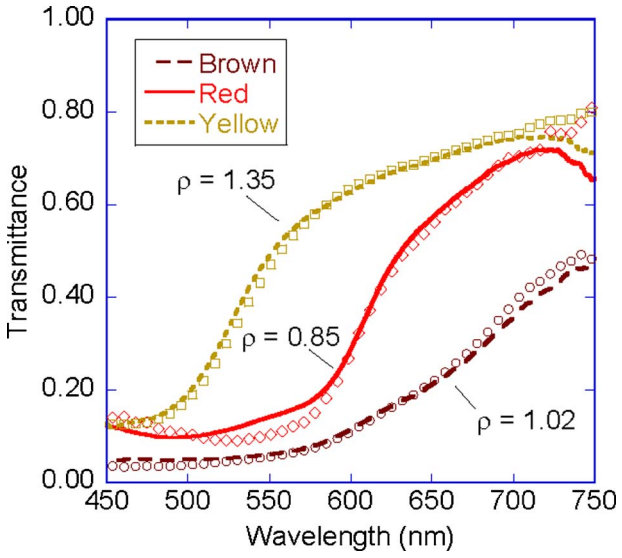

Fig. 5. (Color online) Examples of model fits to specific chromatophore transmittance measurements of the squid *Loligo pealeii* obtained by using K and S values in Fig. 3 and adjusting the scaling parameter ρ. These data are *not* from the same samples given in Fig. 4.

seen in Fig. 3(b) for the squid chromatophore. The absorption spectra of both Cadmium Yellow Light and the squid yellow chromatophore have a rolloff toward the red beginning at ~500 nm, although it is much steeper for the inorganic pigment. The $S(\lambda)$ spectra are much different for these two, however, rising nearly monotonically toward the blue in Fig. 3(b), but low in the blue end of the spectrum and rising sharply at ~500 nm for Cadmium Yellow Light. Again, this pigment was evidently designed as a high yellow reflector (~40% for an 11 μm film [20], whereas typically $R<5\%$ for the yellow chromatophore of *L. pealeii* [6]). Finally, assuming $d\sim1$ μm as a typical thickness for expanded chromatophores [17], the maximum absorption coefficient would be approximately 3 μm^{-1}, which is as great as an order of magnitude larger than K for the inorganic pigments. However, the backscattering coefficients would be in the range of ~0.05–0.08 μm^{-1} in the region of minimum absorption, which is generally smaller than the maximum S of the inorganic pigments (with the exception of Acra Red, a low-reflectance pigment) [6,20]. We conclude that the chromatophores function more effectively as color absorptive filters than colored reflectors. The biological significance of this is possibly that, in some patterns, chromatophores filter light reflected from structures beneath them to fine-tune a particular body pattern.

Since the absorption of the brown pigment is large, it strongly filters light transmitted to and reflected from other elements beneath it. Hence, regardless of the number of elements in the skin structure, the brown chromatophore largely determines the reflected spectrum when it is present (i.e., the skin will appear brown). Light is only partially filtered by the red and yellow chromatophores. Consequently, components beneath them more prominently affect the overall reflection spectrum.

B. Iridophores

Reflection spectra were collected for the red dorsal iridophore of the squid *L. pealeii*. The iridophores in this area of the mantle are parallel to the skin [12]. The angle of incidence in air was approximately 10°. A comparison of iridophore model calculations to these experimental data is given in Fig. 6. The angle of incidence in water is taken to be 7.5°.

For these calculations we have selected $N=20$, a typical number of platelets in the iridophores of squid. We also let $h_L=75$ nm and $h_H=140$ nm, which are within the experimental error of red iridophore spacer and platelet measurements performed by transmission electron microscopy on the squid *Lolliguncula brevis* [23]. Other parameter selections were $f_0=0.4$, $\sigma_\zeta=2.4$ nm, and $\sigma_0=7.6$ nm. We see that $\sigma_\zeta \ll \lambda$ and that the standard deviation σ_0 of spacer thickness over the ensemble of iridophores is about 10% of the mean.

The theoretical plots in Fig. 6 illustrate the effects of the random variables. The ideal stack yields a peak that is too large, having several sidelobes and a general shape that is inconsistent with the data. Introducing a random spacing over the ensemble of iridophores washes out the sidelobes and lowers the peak reflectance. Further randomizing the layer spacings of each iridophore has a minimal effect on the peak and width of the reflection band

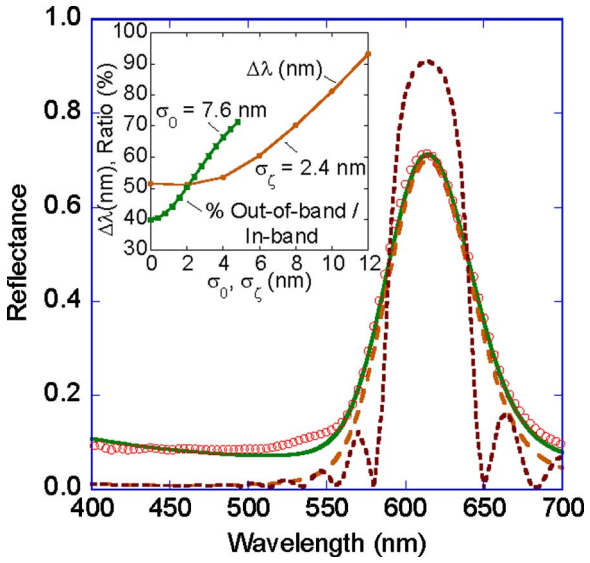

Fig. 6. (Color online) Fit of iridophore model to reflectance data from the red dorsal iridophore of the squid *Loligo pealeii*. The dotted curve gives the calculated spectrum of an ideal thin-film stack (Bragg reflector), while the dashed curve illustrates the effect of averaging over an ensemble of Bragg reflectors with randomly variable mean spacer thickness. The solid curve shows the effects of additionally averaging over individual random spacing of each spacer layer and provides a good fit to the data (circles). The inset shows the dependence of bandwidth $\Delta\lambda$ on σ_0 and the ratio of out-of-band to in-band integrated reflectance on σ_ζ.

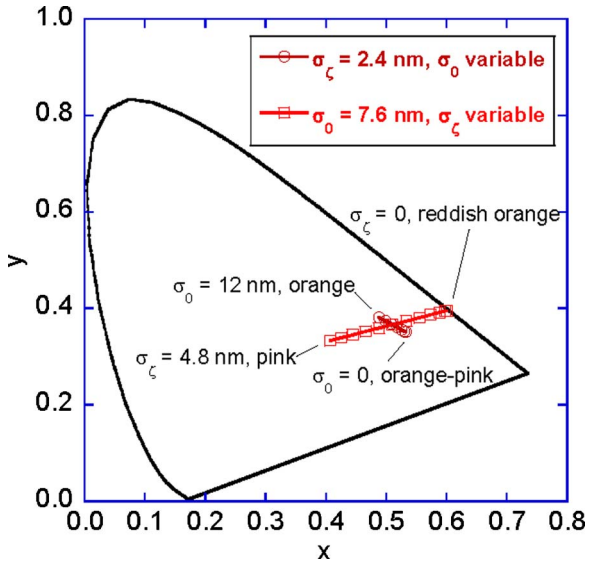

Fig. 7. (Color online) Theoretical chromaticity coordinates for the iridophore of Fig. 6 for various values of the statistical parameters σ_0 and σ_ζ. Also shown is the CIE 1931 chromaticity diagram. CIE standard daylight illuminant D65 was used for these calculations. Circles represent various σ_0 values, ranging from 0 to 12 nm, for a constant σ_ζ=2.4 nm. Squares represent various σ_ζ values, ranging from 0 to 4.8 nm, for a constant σ_0=7.6 nm.

but raises the baseline. The net result is in excellent agreement with the data (circles).

The statistical parameters σ_0 and σ_ζ have a direct impact on coloration effects of the iridophores. As the inset to Fig. 6 shows, the bandwidth $\Delta\lambda$ of the calculated reflectance, defined as the full width of the reflection notch at half-maximum reflectance (FWHM), increases as σ_0 increases for constant σ_ζ. For reference, $\Delta\lambda$=50.8 nm for the ideal Bragg reflector. The random platelet spacing has a somewhat different effect. Since increasing σ_ζ causes the baseline reflectance to rise while having a very minor effect on the peak, we consider the integrated spectral reflectance in band and out of band. The former is obtained by integrating $R_{cc}(\lambda)$ over $\Delta\lambda$ about the peak reflectance, while the latter is given by the integration over the remainder of the spectrum, excluding $\Delta\lambda$. The inset to Fig. 6 shows how the ratio of the out-of-band to in-band integrated reflectance varies with σ_ζ for constant σ_0. For reference, this ratio is 21.2% for the ideal Bragg reflector. We also note that these statistical parameters have relatively minor polarization effects, and these can only be observed at high angles of incidence.

To assess the coloration effects, we plot the chromaticity coordinates for these cases of variable σ_0 and σ_ζ in Fig. 7. For these calculations we have used the CIE 1931 color matching functions and D65 standard daylight illuminant. Variation of σ_0 results in a color perception shift from orange-pink to orange, while that for σ_ζ manifests a color change from reddish orange to pink. The pink color will get fainter as σ_ζ continues to increase, and we anticipate that the iridophore will take on a silvery appearance for large σ_ζ. We emphasize that these coloration effects correspond to what a standard human observer would see for squid near the surface of clear water. For deeper water, the illuminant spectrum would need to be modified based on the spectral attenuation coefficients of the water [27].

A partially active dorsal iridophore was treated with acetylcholine *in vitro*, and the change in the reflection spectrum was observed over time. These data are shown in Fig. 8. Over a period of 60 s the peak reflection doubles and shifts ~50 nm to the blue. We model this using Eqs.

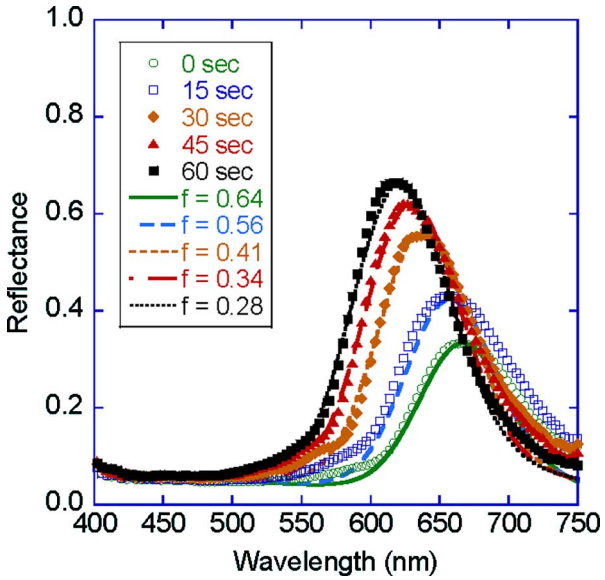

Fig. 8. (Color online) Theoretical reflectance plots and experimental data for an active iridophore treated with acetylcholine (ACh). The points show the measured spectra at various times after application of ACh. The curves are fits to the data obtained from a dynamic iridophore model by adjusting the volume fraction f of water in the platelet regions of the iridophore.

(17) and (18) in the following way. First, we determine parameters for the case of optimum reflection (i.e., at 60 s). For this we set $h_0=139.6$ nm, $f_0=0.28$, $\sigma_\zeta=2$ nm, and $\sigma_0=11$ nm to develop a good fit to the data. As before, $h_L=75$ nm, $\theta_{inc}=7.5°$, and $N=20$. Notice that the volume fraction of water is smaller and the standard deviation σ_0 is larger than those for the fit in Fig. 6. The reason for this is that spectra in Fig. 8 are somewhat broader. Next we selected a value of $dh/df=69.1$ nm. This is consistent with a cutoff of iridophore reflectance at ~700 nm, i.e., the peak wavelength of the iridophore reflection spectrum just before it is extinguished [6]. Finally, we adjusted the volume fraction f, as given in Fig. 8, to fit the calculated spectra to the data. The results are in good agreement with the measured spectra. There does appear to be some asymmetric broadening of the spectral reflection data toward the red as the peak decreases, not accounted for in the model, which could possibly indicate the development of a quadratic chirp in the grating [28]. Since Eqs. (17) and (18) are in simultaneous agreement with all of the data sets using reasonable fitting parameters, we conclude that, to a good approximation, the refractive index and the thickness of the platelets depend linearly on the volume fraction of water (or waterlike fluid) present in the platelet regions.

C. Chromatophore Over Iridophore

We give now an example of a combination spectrum by overlaying a red chromatophore on a blue iridophore. The results are shown in Fig. 9. For these calculations we selected $\rho=1$ and $\xi=0.7$ for the red chromatophore. This value of the forward scattering ratio is typical for diffuse reflectors [19,21]. For the iridophore $h_H=90$ nm, $h_L=71$ nm, $f_0=0.3$, $N=20$, $\sigma_\zeta=2.4$ nm, and $\sigma_0=7.6$ nm. The total reflection spectrum (specular plus diffuse) is in good qualitative agreement with optical measurements of this type of chromatophore–iridophore combination [6]. The chromaticity diagram of Fig. 10 illustrates the type of dynamic color changes that squid can use for camouflage and communication. As the chromatophore expands over the iridophore (given by the circles in Fig. 10 for increasing ρ, assuming that the chromatophore always fills the field of view), the skin color gradually changes from pink ($\rho=0.5$) to purplish pink ($\rho=1$). This is also in agreement with color photos of this chromatophore-iridophore combination [6]. As the chromatophore continues to expand, the color would shift to purplish blue and eventually to blue for $\rho=2$ or 3. These changes may occur within a fraction of a second. Note that the color for $\rho=3$ is virtually indistinguishable from that of a bare iridophore. However, the overlaid chromatophore will produce a diffuse component of the blue reflection, due to scattering in the chromatophore, that is relatively insensitive to viewing angle, unlike the bare iridophore, which produces a purely specular reflection. A physiological change of the iridophore to a noniridescent state, which occurs over several seconds, would produce the color change given by the squares in Fig. 10, with the parameter f increasing in equal increments from 0.3 to 0.9 for $\rho=1.8$. In this case, the skin color passes through various areas (blue, green, yellow, orange, pink) of the chromaticity diagram. The case of $f=0.9$ is virtually indistinguishable from that of a bare chromatophore. Combinations of other iridophores, some situated at large angles with respect to the skin, and chromatophores lead to a rich repertoire of intensity, color, and body patterns available to the animal for adaptation to different backgrounds and situations.

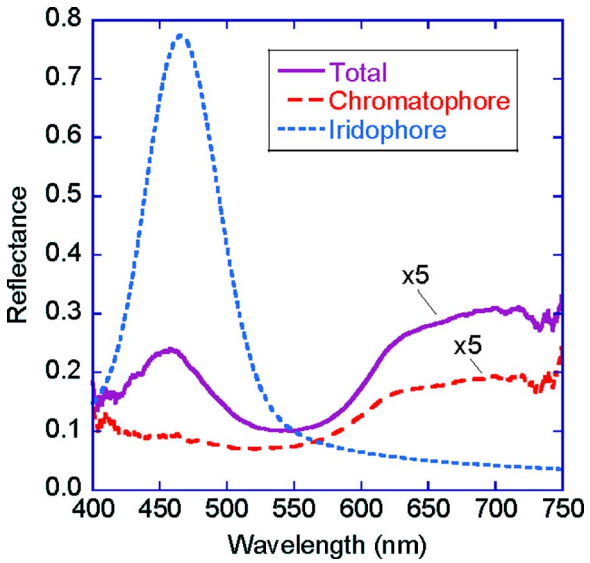

Fig. 9. (Color online) Calculated reflection spectra for a red chromatophore, a blue iridophore, and the combination of a red chromatophore over a blue iridophore. The chromatophore and total reflectance spectra have been multiplied by a factor of 5 for ease of viewing.

5. CONCLUSIONS

In summary, we have presented coloration models applicable to the pigment-bearing chromatophores and iridescent iridophores of squid skin. Dynamic effects have been

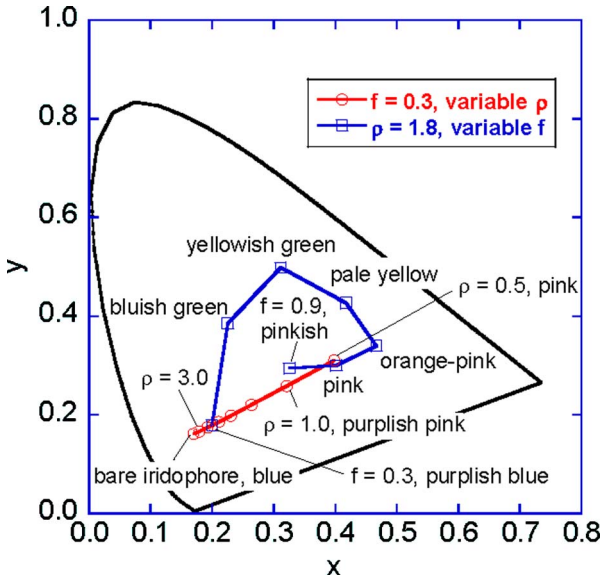

Fig. 10. (Color online) Theoretical chromaticity coordinates for a blue iridophore overlaid with a red chromatophore illustrating color changes for various values of ρ and f. Also shown is the CIE 1931 chromaticity diagram. CIE standard daylight illuminant D65 was used for these calculations. Circles represent various ρ values, ranging from 0.5 to 3, for a constant $f=0.3$. The leftmost circle represents a bare iridophore. Squares represent various f values, ranging from 0.3 to 0.9, for a constant $\rho=1.8$.

included. Calculated spectra agree very well with *in vitro* optical measurements of squid skin components, and combination reflection spectra, for example, a chromatophore overlaid on an iridophore, also agree qualitatively with experimental data. Chromatophores yield low diffuse reflectance due to small backscattering coefficients, but their strong absorption allows fine-tuning of spectral reflections from skin components beneath them. The intensity of these reflections can change in fractions of a second by expansion or retraction of the chromatophore, which can be modeled by the adjustment of a single scaling parameter (ρ). The color and intensity of iridophores can be changed reversibly by a mechanism that seemingly allows invasion of the platelet regions with a waterlike fluid. These changes depend simply on the volume fraction (f) of this fluid. Cephalopods exert direct control over these parameters. Varying just these two control parameters (ρ and f), we have shown that skin color for a chromatophore–iridophore combination can be changed dramatically in a time scale from a fraction of a second to several seconds. A future paper will combine these properties of squid with models and data from cuttlefish for other skin components to obtain a full-skin coloration model for a generic cephalopod. This study provides the physical basis for an improved understanding of the behavioral ecology of these animals.

APPENDIX A

In this appendix we present the solutions to Eqs. (1a)–(1c), yielding expressions for the partial transmittances and reflectances of the chromatophores. Equation (1a) can be integrated immediately, giving

$$I_c(z) = I_{c,0} \exp[-(\alpha+\sigma)z]. \tag{A1}$$

Setting $z=d$ in Eq. (A1) and forming the ratio $I_c(d)/I_c(0)$, we obtain Eq. (2) for T_{cc}. Now substitute Eq. (A1) into Eq. (1b) and differentiate the resulting equation. After combining the result with Eqs. (1b) and (1c), a simple second-order differential equation is obtained:

$$I_d'' - \eta^2\kappa^2 I_d = -\beta_I I_c, \tag{A2}$$

where

$$\beta_I = \sigma\{\xi(\alpha+\sigma) + \eta[\xi\alpha + (1-\xi)\sigma]\}. \tag{A3}$$

Performing a similar set of operations on Eq. (1c), we obtain the second-order differential equation for J_d:

$$J_d'' - \eta^2\kappa^2 J_d = -\beta_J I_c, \tag{A4}$$

with

$$\beta_J = \sigma(\eta-1)(1-\xi)(\alpha+\sigma). \tag{A5}$$

Equations (A2) and (A4) have the general solutions

$$I_d = A_1 e^{\eta\kappa z} + A_2 e^{-\eta\kappa z} + \frac{\beta_I I_c}{(\eta\kappa)^2 - (\alpha+\sigma)^2}, \tag{A6}$$

and

$$J_d = B_1 e^{\eta\kappa z} + B_2 e^{-\eta\kappa z} + \frac{\beta_J I_c}{(\eta\kappa)^2 - (\alpha+\sigma)^2}, \tag{A7}$$

respectively. Integration constants A_1, A_2, B_1, and B_2 can be found by applying the boundary conditions $I_d(0)=I_{d,0}$, $J_d(d)=0$, and the expressions for $I_d'(0)$ and $J_d'(0)$ resulting from Eqs. (1b) and (1c) to Eqs. (A6) and (A7). After some long and tedious but straightforward algebra, we find an expression for $J_{d,0}=J_d(0)$ and form the ratio

$$R_d = \frac{J_{d,0}}{I_{c,0}+I_{d,0}} \equiv (1-q)R_{dd} + qR_{cd}, \tag{A8}$$

where $q=I_{c,0}/(I_{c,0}+I_{d,0})$. Here R_{dd} is given by Eq. (4), and

$$R_{cd} = \frac{b_1 \cosh\eta\kappa d - b_2 \sinh\eta\kappa d}{\eta[(\eta\kappa)^2-(\alpha+\sigma)^2]\{\kappa\cosh\eta\kappa d + [\alpha+(1-\xi)\sigma]\sinh\eta\kappa d\}}, \tag{A9}$$

$$b_1 = \eta\beta_J\{\kappa - [\kappa+\alpha+(1-\xi)\sigma]e^{-(\alpha+\sigma-\eta\kappa)d}\}, \tag{A10}$$

$$b_2 = \{\beta_J[\alpha+\sigma-\eta(\kappa+\alpha+(1-\xi)\sigma)e^{-(\alpha+\sigma-\eta\kappa)d}] - (1-\xi)\sigma[(\eta\kappa)^2-(\alpha+\sigma)^2]\}. \tag{A11}$$

In the limit $\eta\to 1$, $\beta_J\to 0$ and Eq. (A9) reduces to Eq. (7).

Similarly, forming the ratio

$$T_d = \frac{I_d(d)}{I_{c,0}+I_{d,0}} \equiv (1-q)T_{dd} + qT_{cd}, \tag{A12}$$

where T_{dd} is given by Eq. (3), and

$$T_{cd} = a_1\sinh\eta\kappa d - a_2\cosh\eta\kappa d + a_3\sinh^2\eta\kappa d + \frac{\beta_I e^{-(\alpha+\sigma)d}}{(\eta\kappa)^2-(\alpha+\sigma)^2}, \tag{A13}$$

$$a_1 = \frac{\xi\sigma[(\eta\kappa)^2-(\alpha+\sigma)^2]+\beta_I(\alpha+\sigma)}{\eta\kappa[(\eta\kappa)^2-(\alpha+\sigma)^2]} + \frac{\beta_J(1-\xi)\sigma}{\kappa[(\eta\kappa)^2-(\alpha+\sigma)^2]} \times\left\{1-e^{-(\alpha+\sigma-\eta\kappa)d} - \left[\frac{\{\alpha+\sigma-\eta\kappa e^{-(\alpha+\sigma-\eta\kappa)d}+\eta[\alpha+(1-\xi)\sigma](1-e^{-(\alpha+\sigma-\eta\kappa)d})\}\sinh\eta\kappa d}{\eta\kappa\cosh\eta\kappa d+\eta[\alpha+(1-\xi)\sigma]\sinh\eta\kappa d}\right]\right\}, \tag{A14}$$

$$a_2 = \frac{\beta_I}{(\eta\kappa)^2 - (\alpha+\sigma)^2}, \tag{A15}$$

$$a_3 = \frac{(1-\xi)^2\sigma^2}{\eta\kappa \cosh \eta\kappa d + \eta[\alpha+(1-\xi)\sigma]\sinh \eta\kappa d}. \tag{A16}$$

In the limit $\eta \to 1$, Eq. (A13) reduces to Eq. (6).

APPENDIX B

In Eq. (20) we gave an expression for the collimated–collimated transmittance of an iridophore in terms of an integral over $N+1$ random variables. Here we present an approximation that reduces Eq. (20) to an integration over a single random variable. Let $\tau = 1/P_{11}$ be the transmission coefficient, and $\tau = \tau(\zeta_0, \{\zeta_k\})$ is a function of the $N+1$ random variables. Then if we let $\Delta\tau(\zeta_0, \{\zeta_k\}) = \tau(\zeta_0, \{\zeta_k\}) - \tau_0$, where $\tau_0 = \tau(\zeta_0, \{\zeta_k\}=0)$, we can write the multilayer-film transmittance as

$$T_{mf}(\zeta_0, \{\zeta_k\}) = T_0 + 2\,\mathrm{Re}(\tau_0^* \Delta\tau + \Delta\tau^* \Delta\tau), \tag{B1}$$

where $T_0 = \tau_0^* \tau_0$ (for $n_s = n_0$) and the asterisk indicates complex conjugate; T_0 is the multilayer-film transmittance of an ideal stack, where the low-index layer has a thickness $h_L + \zeta_0$ and is computed using Eqs. (13)–(18).

We now expand $\Delta\tau$ in a Taylor series,

$$\Delta\tau(\zeta_0, \{\zeta_k\}) = \sum_{k=1}^{N} \sum_{m=1}^{\infty} \frac{1}{m!} \left(\frac{\partial^m \Delta\tau}{\partial \zeta_k^m} \right)_{\{\zeta_k\}=0} \zeta_k^m. \tag{B2}$$

The partial derivatives in Eq. (B2) will be given in terms of $\partial^m P_{11}/\partial \zeta_k^m$, which can operationally be obtained by differentiating the matrix expressions

$$\frac{\partial^m}{\partial \zeta_k^m} \mathbf{P}(\{\zeta_k\}) = \mathbf{F}_{LH}\mathbf{\Phi}_H\mathbf{F}_{HL}\mathbf{D}(\zeta_1)\mathbf{\Phi}_L\mathbf{F}_{LH} \ldots \mathbf{\Phi}_H\mathbf{F}_{HL} \times \frac{\partial^m}{\partial \zeta_k^m}\mathbf{D}(\zeta_k)\mathbf{\Phi}_L\mathbf{F}_{LH} \ldots \mathbf{\Phi}_H\mathbf{F}_{HL}\mathbf{D}(\zeta_N)\mathbf{\Phi}_L \tag{B3}$$

and

$$\left. \frac{\partial^m \mathbf{D}}{\partial \zeta_k^m} \right|_{\zeta_k=0} = \begin{bmatrix} (-i2\pi n_L/\lambda)^m & 0 \\ 0 & (+i2\pi n_L/\lambda)^m \end{bmatrix}. \tag{B4}$$

Substituting Eq. (B2) into (B1) and using Eq. (B3) and (B4), the integral in Eq. (20) over the N random variables $\{\zeta_k\}$ can be performed term by term. Since we have assumed the variables to be statistically independent, terms like $\langle \zeta_k^m \zeta_{k'}^{m'} \rangle = \langle \zeta_k^m \rangle \langle \zeta_{k'}^{m'} \rangle$ (for $k \neq k'$), where the brackets imply averaging over the corresponding variables. Moreover, for Gaussian statistics only even values of m survive, and $\langle \zeta_k^m \rangle = 1 \cdot 2 \cdot 3 \ldots (m-1)\sigma_k^m$. We let $\sigma_k \equiv \sigma_\zeta$ for all k. Since by Eq. (B4) the mth order term will be proportional to $(\sigma_\zeta/\lambda)^m$, we can ignore all terms of order higher than $m = 2$ when $\sigma_\zeta \ll \lambda$.

It turns out that a Taylor series expansion in terms of ζ_0 does not work as well since the derivatives of τ with respect to ζ_0 are rather large near the zero crossings of τ. Hence, many more terms in the expansion would have to be included. It is thus simpler to integrate over ζ_0 numerically. The final expression for T_{cc} is then given by

$$T_{cc} = \langle T_{mf} \rangle = \overline{T_0} + 2\,\mathrm{Re}(\overline{\tau_0^* \langle \Delta\tau \rangle}), \tag{B5}$$

$$\overline{T_0} = \int_{-\infty}^{\infty} T(\zeta_0) p(\zeta_0) d\zeta_0, \tag{B6}$$

$$\overline{\tau_0^* \langle \Delta\tau \rangle} = \frac{1}{2} \sum_{k=1}^{N} \int_{-\infty}^{\infty} \tau_0^*(\zeta_0) \left. \frac{\partial^2 \Delta\tau(\zeta_0, \{\zeta_k\})}{\partial \zeta_k^2} \right|_{\{\zeta_k\}=0} \sigma_\zeta^2 p(\zeta_0) d\zeta_0, \tag{B7}$$

with

$$p(\zeta_0) = \frac{1}{\sqrt{2\pi}\sigma_0} \exp\left(-\frac{\zeta_0^2}{2\sigma_0^2} \right). \tag{B8}$$

ACKNOWLEDGMENTS

We gratefully acknowledge DARPA and the Air Force Research Laboratory for their support of this work. We also thank Phil McFadden, Rajesh Naik, and Timothy Bunning for stimulating discussions.

REFERENCES

1. P. Vukusic and J. R. Sambles, "Photonic structures in biology," Nature **424**, 852–855 (2003).
2. A. R. Parker, "515 million years of structural colour," J. Opt. A, Pure Appl. Opt. **2**, R15–R28 (2000).
3. A. R. Parker and H. E. Townley, "Biomimetics of photonic nanostructures," Nat. Nanotechnol. **2**, 347–353 (2007).
4. R. T. Hanlon and J. B. Messenger, *Cephalopod Behaviour* (Cambridge U. Press, 1996).
5. R. T. Hanlon, "Cephalopod dynamic camouflage," Curr. Biol. **17**, R400–R404 (2007).
6. L. Mäthger and R. T. Hanlon, "Malleable skin coloration in cephalopods: selective reflectance, transmission and absorbance of light by chromatophores and iridophores," Cell Tissue Res. **329**, 179–186 (2007).
7. C.-C. Chiao and R. T. Hanlon, "Cuttlefish camouflage: visual perception of size, contrast and number of white squares on artificial checkerboard substrata initiates disruptive coloration," J. Exp. Biol. **204**, 2119–2125 (2001).
8. L. M. Mäthger and R. T. Hanlon, "Anatomical basis for camouflaged polarized light communication in squid," Biol. Lett. **2**, 494–496 (2006).
9. J. B. Messenger, "Cephalopod chromatophores: neurobiology and natural history," Biol. Rev. **76**, 473–528 (2001).
10. M. B. Masthay, "Color changes induced by pigment granule aggregation in chromatophores: a quantitative model based on Beer's law," Photochem. Photobiol. **66**, 649–658 (1997).
11. E. J. Denton and M. F. Land, "Mechanism of reflection in silvery layers of fish and cephalopods," Proc. R. Soc. London, Ser. A **178**, 43–61 (1971).
12. L. M. Mäthger and E. J. Denton, "Reflective properties of iridophores and fluorescent 'eyespots' in the loliginid squid *Alloteuthis subulata* and *Loligo vulgaris*," J. Exp. Biol. **204**, 2103–2118 (2001).
13. W. J. Crookes, L. Ding, Q. L. Huang, J. R. Kimbell, J. Horwitz, and M. J. McFall-Ngai, "Reflectins: the unusual proteins of squid reflective tissues," Science **303**, 235–238 (2004).
14. K. M. Cooper and R. T. Hanlon, "Correlation of iridescence with changes in iridophore platelet ultrastructure in the

squid *Lolliguncula brevis*," J. Exp. Biol. **121**, 451–455 (1986).
15. C. D. Mobley, "The optical properties of water," in *Handbook of Optics, Vol. II*, M. Bass, E. W. Van Stryland, D. R. Williams, and W. L. Wolfe, eds. (McGraw-Hill, 1995), Chap. 43.
16. B. Maheu, J. N. Letoulouzan, and G. Gouesbet, "Four-flux models to solve the scattering transfer equation in terms of Lorenz–Mie parameters," Appl. Opt. **23**, 3353–3362 (1984).
17. R. A. Cloney and S. L. Brocco, "Chromatophore organs, reflector cells, iridocytes and leucophores in cephalopods," Am. Zool. **23**, 581–592 (1983).
18. P. Kubelka, "New contributions to the optics of intensely light-scattering materials. Part I," J. Opt. Soc. Am. **38**, 448–457 (1948).
19. R. Levinson, P. Berdahl, and H. Akbari, "Solar spectral optical properties of pigments—part I: model for deriving scattering and absorption coefficients from transmittance and reflectance measurements," Sol. Energy Mater. Sol. Cells **89**, 319–349 (2005).
20. R. Levinson, P. Berdahl, and H. Akbari, "Solar spectral optical properties of pigments—part II: survey of common colorants," Sol. Energy Mater. Sol. Cells **89**, 351–389 (2005).
21. W. E. Vargas and G. A. Niklasson, "Forward-scattering ratios and average pathlength parameter in radiative transfer models," J. Phys.: Condens. Matter **9**, 9083–9096 (1997).
22. K. M. Cooper, R. T. Hanlon, and B. U. Budelmann, "Physiological color change in squid iridophores. II. Ultrastructure mechanisms in *Lolliguncula brevis*," Cell Tissue Res. **259**, 15–24 (1990).
23. R. M. Kramer, W. J. Crookes-Goodson, and R. R. Naik, "The self-organizing properties of squid reflectin protein," Nat. Mater. **6**, 533–538 (2007).
24. H. A. Macleod, *Thin-Film Optical Filters*, 2nd ed. (McGraw-Hill, 1989).
25. M. Born and E. Wolf, *Principles of Optics*, 5th ed. (Pergamon, 1975).
26. L. Mäthger, T. F. T. Collins, and P. A. Lima, "The role of muscarinic receptors and intracellular Ca^{2+} in the spectral reflectivity changes of squid iridophores," J. Exp. Biol. **207**, 1759–1769 (2004).
27. C.-C. Chiao, T. W. Cronin, and D. Osorio, "Color signals in natural scenes: characteristics of reflectance spectra and effects of natural illuminants," J. Opt. Soc. Am. A **17**, 218–224 (2000).
28. H. Kogelnik, "Filter response of nonuniform almost-periodic structures," Bell Syst. Tech. J. **55**, 109–126 (1976).